AGU PUBLICATIONS

JGR

Journal of Geophysical Research: Solid Earth

RESEARCH ARTICLE
10.1002/2017JB014118

Key Points:
- Persistent along-strike directivity of normal-faulting earthquakes in the Apennines
- Evidence of coherent rupture propagation directions along different faults
- Consistency of immediate propagation of seismicity along the main rupture direction

Supporting Information:
- Supporting Information S1

Correspondence to:
G. Calderoni,
giovanna.calderoni@ingv.it

Citation:
Calderoni, G., Rovelli, A., & Di Giovambattista, R. (2017). Rupture directivity of the strongest 2016–2017 central Italy earthquakes. *Journal of Geophysical Research: Solid Earth*, *122*. https://doi.org/10.1002/2017JB014118

Received 21 FEB 2017
Accepted 25 OCT 2017
Accepted article online 27 OCT 2017

Rupture Directivity of the Strongest 2016–2017 Central Italy Earthquakes

Giovanna Calderoni[1], Antonio Rovelli[1], and Rita Di Giovambattista[1]

[1]Istituto Nazionale di Geofisica e Vulcanologia, Rome, Italy

Abstract The along-strike rupture directivity of 16 of the strongest earthquakes ($4.4 \leq M_w \leq 6.5$) within the 2016–2017 central Italy seismic sequence is estimated by investigating high-frequency *S* wave amplitude variations versus source azimuths with an empirical Green's function deconvolution approach. The results confirm that an along-strike rupture directivity is a persistent feature of normal-faulting earthquakes in the Apennines. The preferred rupture directions of the 2016–2017 earthquakes and of similar-magnitude events from the 1997 Umbria-Marche and 2009 L'Aquila-Campotosto seismic sequences show a significant spatial consistency. Different sectors of the Apennines show an alternating trend of preferential along-strike rupture propagation directions with significant spatial and temporal stabilities independent of the magnitude. These results, if confirmed by further data, could lead to more refined hazard assessments of the investigated region.

1. Introduction

On 24 August 2016, a moment magnitude (M_w) 6.0 earthquake struck central Italy that caused the deaths of 296 people and destroyed the small town of Amatrice. Many villages near the epicenter were severely damaged as well (Azzaro et al., 2016). One hour after the earthquake, it was followed by a M_w 5.4 earthquake located 12 km to the NNW. Intense seismic activity consisting of smaller earthquakes ($M_w < 5$) continued for months as aftershocks spread progressively along a NNW-SSE trend over an area ~60 km long and ~20 km wide (Figure 1). On 26 October, two moderate-magnitude earthquakes (M_w 5.4 and 5.9) occurred at the front of the migrating seismicity approximately 30 km NNW of the M_w 6.0 earthquake that occurred on 24 August. Four days subsequent, the largest-magnitude earthquake (M_w 6.5) of the seismic sequence occurred near the town of Norcia between the epicenters of the major 24 August and 26 October earthquakes. This event triggered a strong increase in seismicity throughout an extended area in the Apennines from Amatrice to Camerino that caused large incremental damage to structures that had already been weakened by the previous shocks. The M_w 6.5 earthquake of October 2016 was the largest in Italy since the M_w 6.9 Irpinia earthquake in November 1980. On 18 January 2017, a sharp reactivation of seismicity occurred in the Montereale area to the south of Amatrice (Figure 1); four $M_w \geq 5.0$ earthquakes occurred within 4 h, and several hundreds of aftershocks were recorded within a couple of days. In the entire region affected by the seismic sequence, a total of more than 45,000 $M > 1$ earthquakes were recorded from 24 August 2016 to 31 January 2017, by the National Seismic Network (RSN) operated by the Istituto Nazionale di Geofisica e Vulcanologia (INGV). As of July 2017, seismic activity comprising hundreds of aftershocks per week still persists.

In this study, we investigate the rupture directivity of the nine strongest earthquakes ($M_w \geq 5.0$) and seven smaller-magnitude aftershocks. Rupture propagation is a key feature in earthquake physics, and the rupture directivity has increasingly become the subject of investigation for different types of earthquakes (both shallow and deep, both large and small, and subject to both compressive and extensional regimes) using different analysis methods (e.g., Boatwright, 2007; Folesky et al. 2016; Lengliné & Got, 2011; López-Comino et al., 2016; McGuire, 2004) while also considering complex rupture models in 2-D rupture planes (Park & Ishii, 2015; Poli et al., 2016).

Our analysis is based on empirical Green's function (EGF) deconvolution in the frequency domain, which was used to recognize unilateral along-strike ruptures in Calderoni et al. (2015). Here we improve the method with an extension to bilateral ruptures using the directivity index *D* of Ross and Ben-Zion (2016) to measure the statistical significance. As in previous papers dealing with the 1997 Umbria-Marche and the 2009 L'Aquila normal-faulting earthquakes (Calderoni et al., 2015; Cultrera et al., 2008; Pino, Mazza, & Boschi, 1999), we

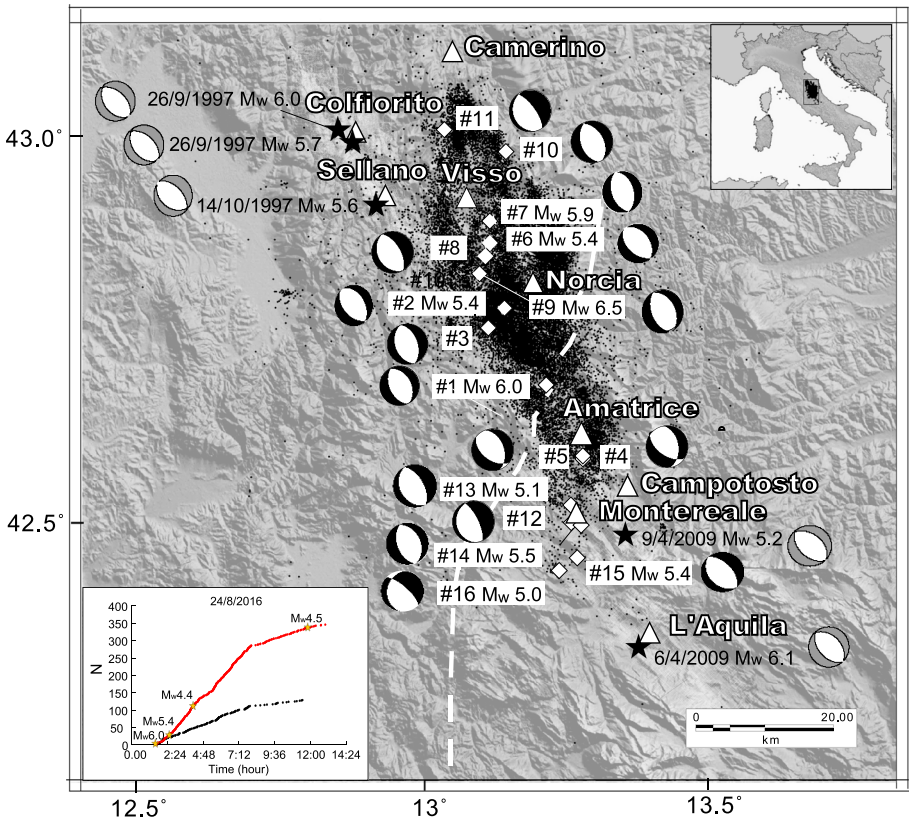

Figure 1. Map of the study area. White diamonds represent the epicenters of the events analyzed in this study, and the adjacent white labels show the event numbers (Table 1). Black stars are the strongest events of the 1997 Umbria-Marche and 2009 L'Aquila-Campotosto seismic sequences. White triangles indicate the most important towns in the study area, and the black dots in the background are the epicenters of the 2016–2017 central Italy seismic sequence. The beach balls represent the fault plane solutions of the earthquakes in the present study (in black) and the strongest shocks in 1997 and 2009 (in gray). The dashed white line is the surface trace of the Sibillini Mountains thrust fault. The inset shows the cumulative number of events in the hours following the 24 August M_w 6.0 destructive earthquake (black to the SSE and red to the NNW).

find a significant persistence of the along-strike directivity in the source ruptures of the 2016–2017 seismic sequence. Unilateral ruptures were predominant (10 out of 16), and only two events did not exhibit directivity. The other four events (including the strongest ones) were characterized by bilateral along-strike ruptures. An alternating predominant direction of rupture propagation is identified along the chain from the northern to the central Apennines.

2. The Study Area

The 2016–2017 seismic sequence in central Italy filled a seismic gap between the northern and central Apennines where the 1997–1998 Umbria-Marche and the 2009 L'Aquila and Campotosto earthquakes occurred, respectively, spanning a total extent of approximately 80 km (Figure 1). At present, the Apennines are characterized by NE-SW striking extension (Carafa & Bird, 2016; Devoti et al., 2011). Moment tensor solutions of the 2016–2017 earthquakes indicate largely prevailing normal-faulting mechanisms consistent with extensional kinematics (http://cnt.rm.ingv.it/tdmt/ and http://www.eas.slu.edu/eqc/eqc_mt/MECH.IT/). The present-day extensional phase followed an earlier compression phase. The Sibillini thrust is widely accepted evidence of a past compressional tectonic regime (see Bigi, Casero, & Ciotoli, 2011; Ghisetti & Vezzani, 1991; Scisciani et al., 2014).

The aftershocks were accurately located using data from the permanent stations of the RSN and from temporary stations installed after the 24 August 2016, M_w 6.0 earthquake (Michele et al., 2016). The aftershocks

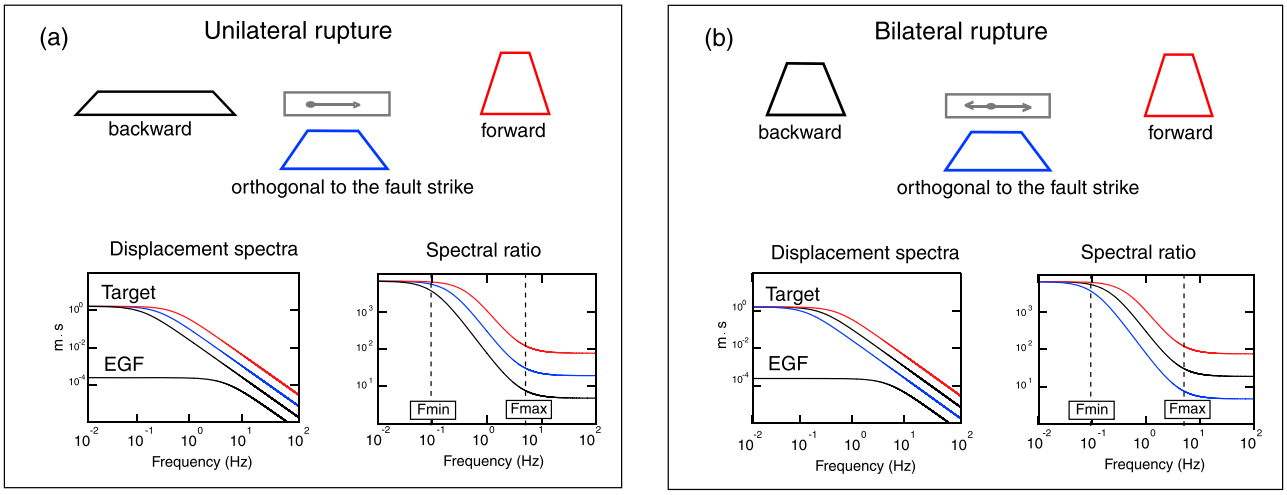

Figure 2. Schematic illustrations of (a) unilateral and (b) bilateral ruptures and the resulting azimuthal variations in the far-field ground motion spectra at different azimuths. The red and black curves represent the amplitude spectra in front and behind the rupture direction, respectively; theblue curve is the amplitude spectrum relative to the fault-orthogonal azimuths. When the target event spectrum is divided by the EGF spectrum, the contribution of the site and propagation path cancel out, and the spectral ratio isolates the effect of the rupture propagation. The relative amplitude of the spectral ratios between the low- and high-frequency asymptotes (the F_{min} to F_{max} frequency range) is an unequivocal indicator of unilateral or bilateral rupturing; the fault-orthogonal curve is intermediate for a unilateral rupture while it is minimal for a bilateral rupture.

extended through the Apennines along a system composed of at least two different faults, namely, the Mount Vettore and the Laga Mountains faults, mapped at the surface between Norcia and Campotosto (Galadini & Galli, 2003). Interposed between the two faults is a preexisting structural barrier represented by the lateral ramp of the Sibillini thrust (see Figure 1).

Geological and seismological results combined with surface coseismic deformation estimated from geodetic data (Cheloni et al., 2017; Lavecchia et al., 2016; Pucci et al., 2017) indicate the activation of high-angle SW dipping faults. We use this information to identify which of the two nodal planes is the fault plane that our analysis method is otherwise unable to resolve.

3. Theory

The rupture directivity causes variations in the ground motion at different source azimuths (Ben-Menahem, 1961). For unilateral ruptures, this effect is manifested primarily by shorter-duration, higher-amplitude source time functions in the direction of the rupture propagation and longer-duration, lower-amplitude source time functions in the opposite direction (Figure 2a). For a basic model of a pulse-type rupture (e.g., Haskell, 1964; Hirasawa & Stauder, 1965), the variations in the source duration versus the azimuth are given by

$$T(\theta) = \frac{L}{v_r} - \frac{L\cos\theta}{\beta} = T_0\left(1 - \frac{v_r}{\beta}\cos\theta\right) \quad (1)$$

where L and v_r are the rupture length and velocity, respectively; β is the shear wave velocity; and θ is the angle between the direction of rupture and the recording station. The parameter $T_0 = \frac{L}{v_r}$ corresponds to the duration of the rupture propagation and is observed as the source pulse duration when ϑ is ±90° (Calderoni et al., 2015; Calderoni, Rovelli, & Singh, 2013; Kane et al., 2013). When an omega-square source model is assumed in a far-field approximation (Aki, 1967), the displacement amplitude spectrum will consistently exhibit an azimuth-dependent corner frequency (f_0), which is inversely proportional to the source duration (Figure 2a). Note that the time integral of the source function, which corresponds to the seismic moment, remains invariant for different azimuths. Consistently, in the frequency domain, the amplitudes of the low-frequency displacement spectra are the same for different azimuths.

Using a scheme similar to that of a unilateral rupture, the pulse durations are shorter along both along-strike directions than in the directions orthogonal to the rupture propagation when a rupture is bilateral (Figure 2b).

The spectra behave consistently, where higher corner frequencies are observed along the strike of the rupture. In the case of a bilateral rupture, high-frequency amplitudes are minimal at the stations located orthogonally to the fault (Figure 2b).

These basic spectral properties are used in this paper to investigate the rupture directivity of the 2016–2017 central Italy earthquakes. The analysis is based on the computation of the amplitude variations versus the station azimuths. As shown in Figure 2, the spectrum of the target earthquake is divided by the spectrum of a colocated, smaller-magnitude event (the so-called EGF) under the constraint that both the focal mechanisms and the propagation paths are similar. The resulting spectral ratio (see Figure 2) is characterized by two asymptotes at low and high frequencies that are indicated by F_{min} and F_{max} in Figure 2. This frequency range is controlled by both the target and the EGF corner frequencies as discussed in Calderoni et al. (2013). In this regard, the amplitude variations between F_{min} and F_{max} versus the station azimuths represent the signature of the rupture directivity of the target event.

When the constraints on small source distances and similar focal mechanisms are honored, this method makes no further assumptions on the source and propagation models, and it does not require the computation of additional parameters that are often poorly constrained. Any dependence on various source parameters, such as the corner frequency, stress drop, and local propagation properties, are consequently bypassed. The spectra of target events observed at different azimuths are corrected simply through the EGF spectra with a spectral ratio operation, and the inferred source spectra are correspondingly free of biases that might be produced by adopting idealized source and/or structural models. The possible directivity of the EGF does not affect the directivity estimates for the target events. The directivity of the EGF rupture can scatter F_{max} at different azimuths, but it does not influence the spectral ratio amplitudes between the two asymptotes, and there is no bias if F_{max} is chosen as the smallest of the EGF corner frequencies. Moreover, instrumental corrections are not necessary since the target event and the EGF event at each station are recorded by the same instrument. The along-strike rupture directivity, which is the focus of this work, is determined using only the observed spectra of the target events divided by the EGF spectra from the stations available within the azimuth range of interest. Due to the geographic shape of the Italian peninsula, which is elongated parallel to the Apennines, a good along-strike coverage of stations is guaranteed at large distances; this permits a clear separation between the spectral ratios versus the station azimuths for the directive ruptures according to the schemes shown in Figure 2. In this approach, results regarding the source directivity can be achieved in a short time (on the order of 1 h) after a significant earthquake.

4. Data

The 2016–2017 central Italy seismic sequence was recorded for magnitudes as small as M 1 by 24-bit broadband seismological stations operated by the INGV. The event waveforms (http://eida.rm.ingv.it/) in addition to their hypocentral parameters and magnitudes (http://iside.rm.ingv.it/) are available online.

Immediately after the M_w 6.0 earthquake on 24 August, researchers from the INGV rapidly installed 17 temporary broadband stations in the epicentral area. Similar to the permanent stations, the temporary stations were mostly equipped with 40 s Nanometrics Trillium seismometers at acquisition rates of 100 samples per second (sps). Moreover, the strongest events were also recorded by stations from the strong motion network (RAN) managed by the National Civil Protection Department (DPC). The RAN stations were generally equipped with three-component Kinemetrics EpiSensor accelerometers with a full-scale range of either 1 or 2 g coupled with 24-bit digitizers set to record at 200 sps.

The records (both the raw seismograms and accelerograms) are processed using a procedure similar to that used in Calderoni et al. (2015). The amplitude spectra are computed through a fast Fourier transform in a 10 s time window starting 1 s before the direct S arrival. This window includes the most energetic part of the S phase on both of the horizontal components. The selected time windows are tapered using a conventional Hanning taper in the SAC software suite, and the spectra are smoothed using a 0.1 Hz wide triangular operator in the same package (Goldstein et al., 2003). The resulting amplitude spectrum for each station and each event used in this paper is the square root of the quadratic composition of the two horizontal components.

Table 1
List of Earthquakes (Target Events) for Which the Rupture Directivity Is Investigated

	Target						EGF				
N	Time UTC	Latitude (°)	Longitude (°)	Depth (km)	M_w	Direction type	Time UTC	Latitude (°)	Longitude (°)	Depth (km)	M_w, M_L
1	24/08/2016 01:36	42.698	13.234	8	6.0	B	26/08/2016 04:08	42.698	13.231	11	3.0
2	24/08/2016 02:33	42.794	13.154	9	5.4	U	26/08/2016 20:49	42.794	13.153	10	3.2
3	24/08/2016 04:06	42.769	13.125	8	4.4	U	25/08/2016 02:29	42.763	13.116	8	2.7
4	25/08/2016 12:36	42.596	13.290	10	4.4	C	10/10/2016 23:00	42.588	13.299	10	2.8
5	26/08/2016 04:28	42.600	13.290	11	4.8	C	25/08/2016 13:34	42.605	13.294	10	2.8
6	26/10/2016 17:10	42.880	13.128	9	5.4	U	21/11/2016 03:42	42.886	13.145	9	2.8
7	26/10/2016 19:18	42.909	13.129	8	5.9	B	02/11/2016 05:30	42.914	13.135	10	2.9
8	26/10/2016 21:42	42.863	13.121	10	4.5	U	26/10/2016 17:36	42.866	13.131	8	2.8
9	30/10/2016 06:40	42.840	13.110	9	6.5	B	31/08/2016 11:26	42.832	13.120	10	3.9
10	01/11/2016 07:56	43.000	13.158	10	4.8	U	09/11/2016 05:03	42.998	13.144	6	2.8
11	03/11/2016 00:35	43.029	13.049	8	4.7	U	24/11/2016 18:00	43.039	13.063	9	2.8
12	29/11/2016 16:14	42.529	13.280	11	4.4	U	08/11/2016 21:29	42.551	13.246	10	2.6
13	18/01/2017 09:25	42.547	13.262	9	5.1	U	25/12/2016 17:19	42.556	13.239	10	2.8
14	18/01/2017 10:14	42.529	13.282	9	5.5	U	18/01/2017 12:01	42.534	13.285	11	3.9
15	18/01/2017 10:25	42.494	13.311	9	5.4	B	27/08/2016 08:27	42.465	13.245	11	2.8
16	18/01/2017 13:33	42.477	13.281	10	5.0	U	27/08/2016 08:27	42.465	13.245	11	2.8

Note. The corresponding EGFs are written in the same row. The letters U, B, and C indicate the events that resulted in unilateral, bilateral, and circular ruptures, respectively.

The analyzed events (Table 1) include the nine strongest earthquakes ($M_w \geq 5.0$) of the 2016–2017 central Italy seismic sequence and seven aftershocks in the moment magnitude range $4.4 \leq M_w \leq 4.8$. The events are selected based upon co-located EGFs with good quality waveforms when both the target event and the EGF event are not within the coda of a previous earthquake. The moment magnitudes are taken from http://cnt.rm.ingv.it/tdmt/ or http://www.eas.slu.edu/eqc/eqc_mt/MECH.IT/; when the moment tensor determination is not available, as is the case for the majority of the EGFs (see Table 1), the local magnitudes (M_L) are taken from http://iside.rm.ingv.it.

The EGFs are chosen according to the constraint of being as close as possible to the target while having the same normal-faulting source mechanism. The source distances between the target and EGF events are smaller than 3 km for 88% of the considered target-EGF event pairs, although it ranges from 3 to 5 km for two events. The focal mechanisms of both the target and the EGF events are available for only two pairs due to the limited number of EGFs with moment tensor determinations (events #9 and #14 of Table 1). For these two events, the consistency between the focal mechanisms is guaranteed by a direct comparison between the solutions. For the other target-EGF event pairs, the closeness of the hypocenters suggests that they are likely located on the same fault and consequently have the same rupture mechanism. To support this hypothesis, we perform a check using the polarities of the first arrivals of the target and EGF events at the available stations. We find the same *P*

polarities for 97% of the samples, which honors one of the conditions required; in that, the focal mechanisms must be similar.

5. Analysis Method

The rupture directivity is investigated using unclipped records obtained mostly between 40 and 200 km from the source. This distance range is controlled by the amplitude saturation, which prevents the use of velocity transducer records at closer stations, during the strongest target events. In these cases, the alternative use of strong motion accelerograms is possible; however, only a few accelerometric stations can provide records with acceptable noise conditions for the EGF waveforms at the lowest frequencies. High noise levels also prevent the use of stations located farther away. For an objective station selection process, preevent noise windows with the same duration as the *S* wave windows are used to compute the SNR; for each target-EGF event pair, only stations with a SNR greater than 3 in the frequency range from $F_{\min}$ to $F_{\max}$ are retained for the analysis.

The spectral ratios between the target event and EGF event are then computed for the selected stations for each target-EGF event pair in Table 1. Some examples of these spectral ratios are shown in Figures 3a1–3a4. Further examples can be found in the supporting information. The stations are grouped within angles of ±45° from the fault strike. The colors in Figure 3 distinguish three different groups: red and black spectral ratios represent stations to the NNW and SSE, respectively, while the blue spectral ratios represent fault-orthogonal (FO) stations on either side of the fault. These colors mimic those of the spectral ratios in Figure 2. For each group and for each frequency, the geometric mean ($\overline{X}$) and the standard deviation (s) are computed for the station ensemble; Figures 3b1–3b4 depict the behavior of the band $\overline{X} \pm 1$ s as a function of the frequency. According to Figure 2, three cases are possible: (i) the red and black curves exceed the blue curves, providing evidence for a bilateral rupture; (ii) the blue curves are intermediate between the other two colors, providing evidence for a unilateral rupture; and (iii) all of the three colors overlap, indicating that the rupture was circular in nature.

To determine whether there is a statistically significant difference in the mean spectral separation between the NNW, SSE, and FO groups, the *t* test criterion of Ross and Ben-Zion (2016) is adopted. We calculate the parameter t_{ij} at each frequency value as

$$t_{ij} = \frac{\overline{X_i} - \overline{X_j}}{s_{\overline{X_i} - \overline{X_j}}} \tag{2}$$

$$s_{\overline{X_i} - \overline{X_j}} = \sqrt{\frac{s_i^2}{n_i} + \frac{s_j^2}{n_j}} \tag{3}$$

The above symbols are the same as those in Ross and Ben-Zion (2016) for unilateral along-strike ruptures; however, these symbols are denoted with two subscripts *i* and *j* that extend the application to bilateral ruptures as well:

$$i, j =, 2, 3 \text{ with } i \neq j \tag{4}$$

where 1, 2, and 3 represent the NNW, SSE, and FO groups, respectively. Note that equations (2) and (3) are identical to equations (7) and (8) of Ross and Ben-Zion (2016) when $i, j = 1, 2$, which considers only the two groups of along-strike stations.

Figures 3c1–3c4, 3d1–3d4, and 3e1–3e4 show the values at each frequency for t_{12} (or t_{21}), t_{13}, and t_{23}, respectively, which represent the significance of the spectral separation between the NNW and SSE groups (or between SSE and NNW), between the NNW and FO groups, and between the SSE and FO groups, respectively. Our directivity index D_{ij} is then calculated as the mean of t_{ij} over the frequency band from $F_{\min}$ to $F_{\max}$:

$$D_{ij} = \frac{1}{F\max - F\min} \int_{F\min}^{F\max} t_{ij}(f) df \tag{5}$$

The frequency range $F_{\min}$ to $F_{\max}$ is determined visually. The choice of the two corner frequencies requires some attention, because an exceedingly small value of $F_{\min}$ will tend to underestimate the directivity while

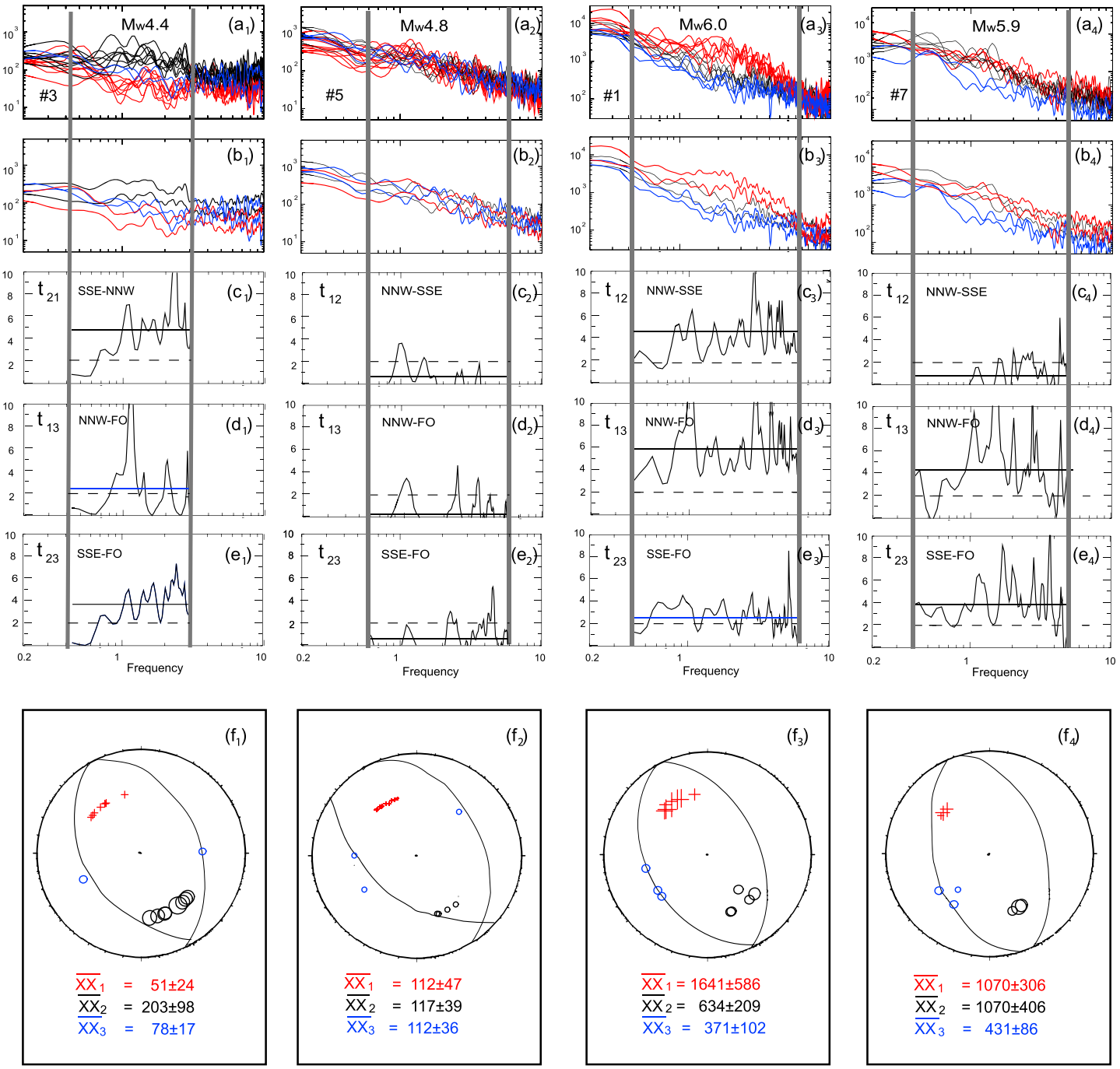

Figure 3. Examples of the step-by-step analysis of the present study. The four columns provide representative target-EGF event pairs. (a1–a4) The azimuthal variations in the individual station spectral ratios at different azimuths (red,black, and blue curves are relative to NNW, SSE, and fault-orthogonal stations, respectively). (b1–b4) The spectral ratio variations are represented through ±1 standard deviation bands around the mean for the different groups of azimuths. (c1–c4, d1–d4, and e1–e4) The *t* curves obtained according to the criterion of Ross and Ben-Zion (2016) that provide the statistical significance of the directivity for the different groups of azimuth. The frequency band limitations (vertical straight lines) bound the range from F_{min} to F_{max}. (f1–f4) The azimuthal variations of the high-frequency amplitudes through the stereonet projection of the station takeoff angles, as first used by Boatwright (2007) for peak ground motions.

an exceedingly large value of F_{max} will cause a bias in the possible directivity of the EGF. However, we verify the variations in D_{ij} when F_{min} and F_{max} are varied; the final choice of the frequency range is determined such that a 20% decrease in F_{min} and a 20% increase in F_{max} will cause a change of less than 10% in D_{ij}.

According to Ross and Ben-Zion (2016), a value of approximately 2.0 for D_{ij} is a reliable threshold for indicating significantly different samples. In Figure 3, the directivity index is represented by the horizontal straight line in the t_{ij} panels, whereas the dashed black line is the statistical threshold of 2.

Figures 3f1–3f4 provide a different visualization of the azimuthal variations in the high-frequency amplitudes due to the rupture directivity using stereonet projections of the station takeoff angles. Boatwright (2007) first introduced this representation of azimuthal variations using peak ground motions to study the rupture directivity. Calderoni et al. (2015) showed that stereonet projections could lead to equivalent conclusions regarding the directivity when peak ground motions or high-frequency spectral ratios in an EGF approach are used. In Figures 3f1–3f4, the symbol size for each station is proportional to the spectral separation computed as the average spectral ratio in the frequency range from $F_{\min}$ to $F_{\max}$. In each panel, $\overline{XX}$ indicates the average value over the station ensemble of each group. Of course, the general observation that emerges from examining the stereonet projections is the same as that of the top plots of each column in Figure 3, but this visualization technique is particularly informative with respect to the possible role of the takeoff angle as discussed in Boatwright (2007). This information is fundamental for constraining the subhorizontal versus the subvertical character of rupture propagation (Poli et al., 2016; Prieto et al., 2017; Warren & Shearer, 2006). In a stereonet visualization, the largest amplitudes at the smallest takeoff angles denote subvertical ruptures (Boatwright, 2007). Employing the 1-D velocity model used to locate the earthquakes and the distance ranges of the stations, the resulting takeoff angles of the stations shown in the stereonet projections of Figure 3 are concentrated in a small range from 35° to 50°.

The stability of the amplitudes observed for all of the takeoff angles suggest that there is no distance variation in the range from 40 to 200 km; this is a strong indication for a significant subhorizontal component within the rupture propagation. However, the station distribution and the use of orthogonal directions, which are optimal for studying the along-strike directivity, are not capable of resolving the updip/downdip directivity. Therefore, in this paper, we limit our assessments to the along-strike directivity.

Another parameter that is not systematically computed in the present study is the rupture velocity, which will be the subject of a future paper. However, based on equation (1), the observed azimuthal variations in the spectral ratios are generally consistent with v_r values of approximately 0.5 β in a horizontal rupture propagation assumption.

6. Results

The approach described in the previous section is applied to the 16 target-EGF event pairs shown in Table 1. Figures 4a and 4b show the final results of the present study. For each event pair, the map in the right-hand side illustrates the stations utilized in this study and the epicenters of the target and EGF events. As in the previous figures, the station colors indicate different station azimuths (red, black, and blue colors correspond to NNW, SSE, and FO directions, respectively). The top plots to the left of each map show the ±1 standard deviation band around the mean at different azimuths (as in Figure 3), and the bottom plots indicate the resulting directivity constrained through the largest D_{ij} value. The curves of t_{ij} are red or black for unilateral ruptures (to the NNW or SSE, respectively), cyan for bilateral ruptures, and gray for circular ruptures. For bilateral ruptures, Table 2 shows the values of D_{ij} that provide the percentages of the ruptures in the opposite directions.

Ultimately, we see that only two events (#4 and #5) can be classified as circular ruptures. Event numbers 2, 3, 6, 8, 10, 11, 12, 13, 14, and 16 are evidently unilateral ruptures; among them, the blue ±1 standard deviation band is intermediate between the red and black curves according to the requirements of Figure 2, and the t_{12} (or t_{21}) curves are clearly greater than 2. The ruptures of the remaining four events (1, 7, 9, and 15) are identified as bilateral; the directivity indices of the two along-strike groups with respect to the FO group are both higher than 2 (Table 2). In three of those cases, the along-strike difference is small, indicating a nearly symmetrical bilateral rupture; in the other case (event #1), there is a clearly NNW trending predominance of the rupture.

We note that the number of events that show a significant rupture directivity is similarly large for moderate and smaller magnitudes, which confirms the findings by McGuire (2004), Boatwright (2007), Seekins and

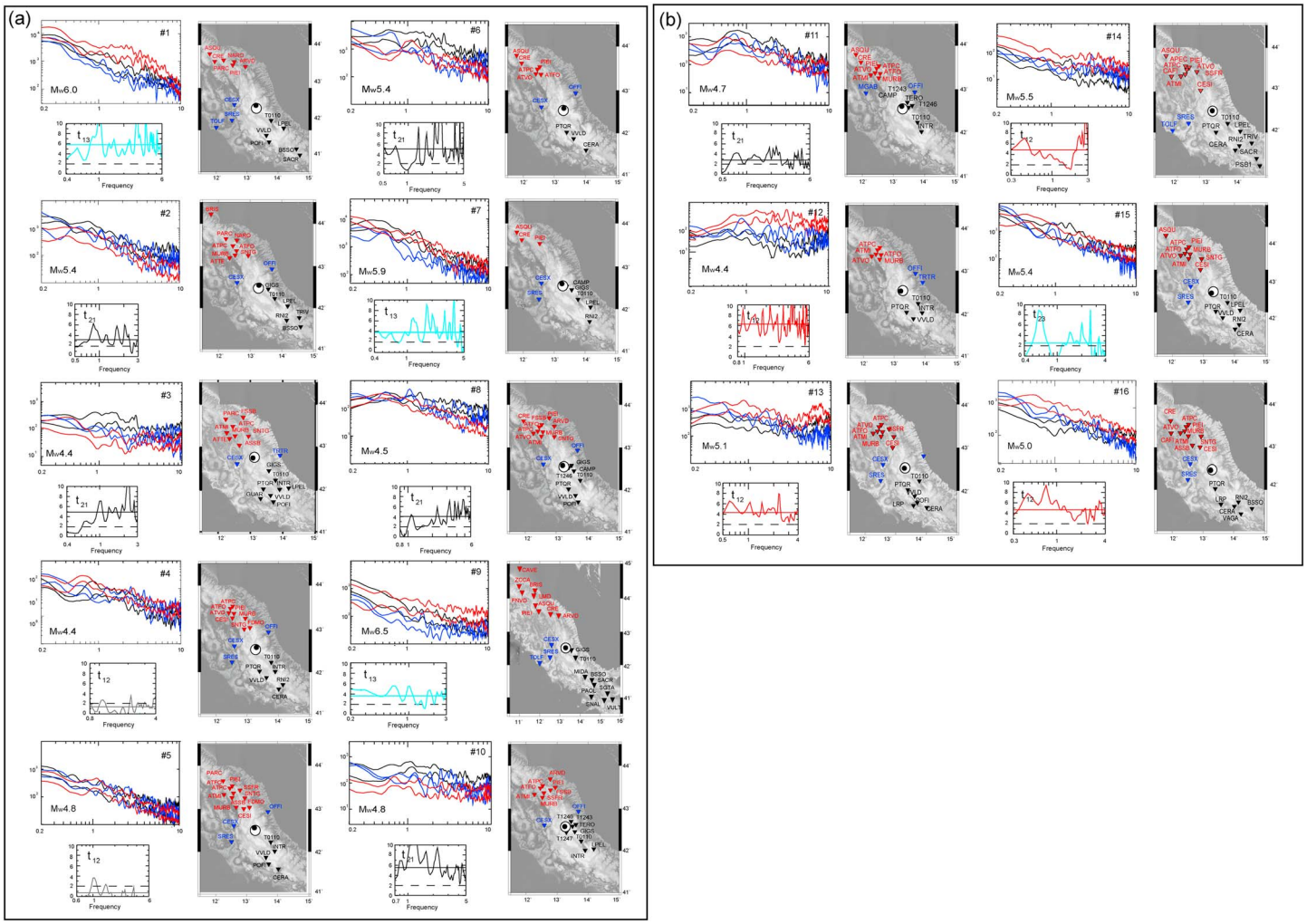

Figure 4. The epicenters for all of the analyzed target and EGF events are represented in a map with white and black circles, respectively. The top left plots show the azimuthal variations in the ±1 standard deviation band around the mean of the spectral ratios at different azimuths (red, black, and blue curves are relative to NNW, SSE, and fault-orthogonal station groups, respectively). In the bottom left plots, the *t* curves provide statistical estimates of the spectral separation between the different directions. Red and black curves indicate the unilateral ruptures toward the NNW and SSE, respectively, while cyan and gray curves indicate the bilateral and circular ruptures, respectively.

Boatwright (2010), Lengliné and Got (2011), Kane et al. (2013), and Calderoni et al. (2013, 2015) regarding the persistency of the directivity even at small magnitudes.

Another result that emerges from Figure 4 is that the two strongest earthquakes of Amatrice and Norcia (events #1 and #9, respectively) both propagated bilaterally; however, they demonstrate different behaviors, as the former propagated mostly toward the NNW and the latter showed a similar rupture percentage in the opposite direction (Table 2). Several details of our results are consistent with the asymmetry of the slip patches found by Tinti et al. (2016) and Tinti et al. (2017) in their rupture history inversions. In particular, during the inversion of the Amatrice M_w 6.0 earthquake (event #1), Tinti et al. (2016) found a large, ~10 km patch of slip that propagated along the fault strike toward the NNW and a smaller patch that propagated in the opposite direction, with an initial updip component that we are not able to resolve here. The temporal history of the slip for the M_w 6.5 Norcia earthquake (event #9) is somewhat more complex (Tinti et al., 2017). However, the results of these studies also suggest a subhorizontal elongation of the slip patch toward the NNW and SSE from the nucleation point for this event.

Finally, Figure 5 shows that a SSE rupture directivity is a common feature for many of the investigated events to the north of Amatrice, including the M_w 5.4 aftershock that occurred less than 1 h after the

Table 2
Statistical Significance of the Azimuthal Amplitude Variations in the Bilateral Ruptures Measured Using the D Index

N	Date	M_w	Stations	D	%
#1	24/08/2016 01:36	6.0	NNW–SSE	4.5	
			NNW–FO	5.8	70%
			SSE–FO	2.5	30%
#7	26/10/2016 19:18	5.9	NNW–SSE	0.7	
			NNW–FO	4.3	53%
			SSE–FO	3.8	47%
#9	30/10/2016 06:40	6.5	NNW–SSE	2.2	
			NNW–FO	4.7	57%
			SSE–FO	3.6	43%
#15	18/01/2017 10:25	5.4	NNW–SSE	0.3	
			NNW–FO	2.4	54%
			SSE–FO	2.1	46%

Note. The percent symbol (%) indicates the percentage of ruptures in the two along-strike directions.

M_w 6.0 earthquake on 24 August 2016. Interestingly, the seismicity pattern immediately following the first strong shock indicates a predominant migration toward the NNW, where the strongest of the early aftershocks occurred within 1 h after the main shock (see the inset in Figure 1). Another two shocks (M_w 4.4 and 4.5) followed a few hours subsequent. The inset in Figure 1 shows that the extent of the early distribution of along-strike seismicity is significantly asymmetrical. As discussed in Rubin and Gillard (2000) and in Zaliapin and Ben-Zion (2011), this could imply a correlation between the direction of the rupture propagation and the immediate seismicity following the main shock, where a higher occurrence probability is observed for earthquakes with significant magnitudes in the along-strike direction of rupture propagation. In this case, both the higher number of early-stage aftershocks toward the NNW and the azimuth of the strongest aftershock that immediately followed the main event are consistent with the direction of rupture propagation during the 24 August 2016, M_w 6.0 Amatrice earthquake.

7. Discussion of the Resulting Directivity Patterns

The existence of a strict correspondence between the along-strike and updip directivity with strike-slip and dip-slip rupture mechanisms, respectively, is widely accepted (see Koketsu et al. (2016) for a discussion). These authors modeled the 2015 Gorka, Nepal, earthquake that occurred within the underthrusting Indian lithosphere and demonstrated that the combination of a low dip angle and a fast rupture velocity would favor a strong along-strike directivity for a dip-slip earthquake. However, an along-strike rupture directivity is also frequently observed along high-angle normal faults. This persistent feature has been repeatedly documented in many papers on moderate-magnitude earthquakes in the Apennines. Pino et al. (1999), Cultrera et al. (2008), and Calderoni et al. (2011) investigated the rupture directivity of the highest-magnitude events ($5.6 \leq M_w \leq 6.0$) of the 1997–1998 Umbria-Marche seismic sequence. Using different methods, they consistently found that the strongest earthquake near Colfiorito (27 September 1997, M_w 6.0) was characterized by a significant directivity toward the NW, whereas the aftershock near Sellano (14 September 1997, M_w 5.6) showed an opposite along-strike rupture propagation direction. Pino et al. (1999) also determined that the rupture directivity of the M_w 5.7 Colfiorito earthquake that occurred on 27 September 1997 was toward the SE. In addition, the 2009 earthquakes around L'Aquila were characterized by a persistency in the along-strike rupture directivity (Calderoni et al., 2015). The Paganica fault, where the main shock (6 April 2009, M_w 6.1) nucleated, and the contiguous at depth San Demetrio fault segment (Calderoni et al., 2012) showed a high (73%) percentage of earthquakes with unilateral ruptures toward the SE. The Campotosto fault, which is subparallel to the Paganica fault and forms a right step with it, showed more variable behavior with a predominance of unilateral ruptures toward the SE along the southern part of the fault and several ruptures propagating toward the NW along the northern part of the fault. It is noteworthy that the Campotosto fault is the closest mapped fault to the south of the fault that generated the 24 August 2016 Amatrice earthquake (Pierantoni, Deiana, & Galdenzi, 2013). These two faults exhibit similar strikes and are aligned with an insignificant offset.

In Figure 5a, we represent the directivity results of this study through colored arrows (red and black colors indicate ruptures toward the NNW and SSE, respectively), where the arrow size is proportional to the directivity index, to visualize the statistical significance of the weighting factors. For both unilateral and bilateral ruptures, the lengths of the red and black arrow segments are scaled to a unique value of D (the largest value is approximately 6). The relative contribution of bilateral ruptures reflects the percentage of ruptures in opposite directions as shown in Table 2.

Figure 5b compares the results of this paper with the rupture directivity results for the 1997 earthquakes near Colfiorito (the thick arrows in the fault plane boxes in the northernmost part of the map in Figure 5b) and for the 2009 L'Aquila and Campotosto earthquakes (thin black and red arrows, respectively, in the southernmost part of the map). The predominant rupture directions of the 24 August 2016, M_w 6.0 earthquake and the

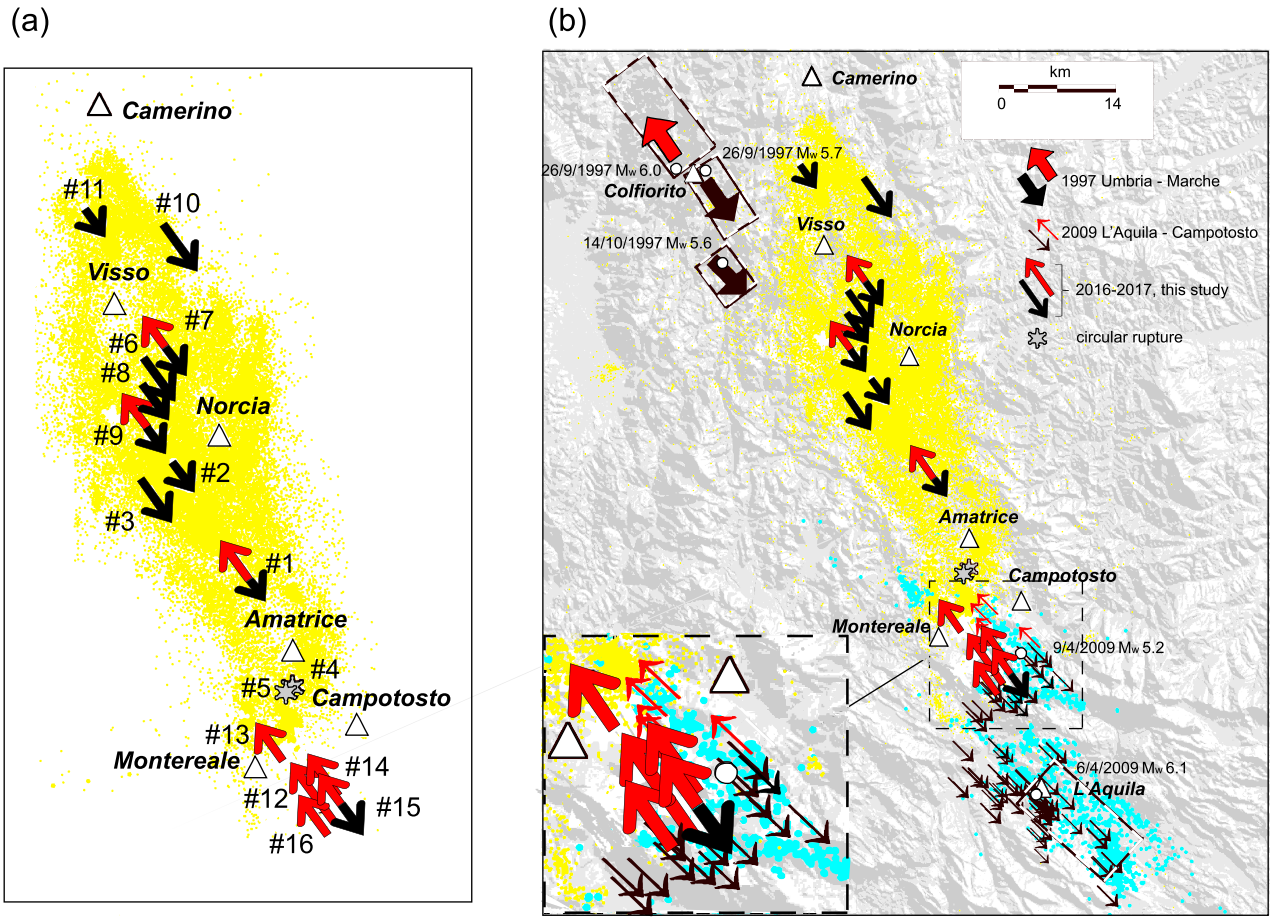

Figure 5. (a) Results for the rupture directivity from the present study. The rupture direction is visualized with red (NNW) and black (SSE) arrows, where the arrow length is proportional to the directivity index. For bilateral ruptures, the relative percentages in opposite directions are those shown in Table 2. Yellow dots in the background are the epicenters of the 2016–2017 central Italy seismic sequence. (b) Along-strike rupture propagation directions available for the normal-faulting earthquakes in the northern and central Apennines. The results refer to three seismic sequences (1997 Umbria-Marche, 2009 L'Aquila-Campotosto, and 2016–2017 Amatrice-Norcia). Rectangles contoured by dashed lines are the surface projections of the ruptured fault planes responsible for the largest earthquakes of the 1997 Umbria-Marche seismic sequence (DISS Working Group, 2015). Yellow and cyan dots represent the epicenters of the 2016–2017 and 2009 seismic sequences, respectively. As in Figure 5a, the rupture directions are represented by red (NNW) and black (SSE) arrows. The magnified view of the dashed black box is for better visualizing the areal consistency in the NNW directivity between the 2009 and 2016–2017 earthquake sequences that occurred along the same portion of the fault system at the northern tip of the Campotosto fault.

earthquakes near Montereale along the Laga Mountains fault are both NNW, which is consistent with the results from five 2009 earthquakes that occurred along the nearby northern tip of the Campotosto fault. A persistent rupture propagation in the opposite direction (SSE) is observed to the north of Amatrice up to Colfiorito, including the strongest 30 October 2016, M_w 6.5 Norcia earthquake. The SSE rupture directivity of the 2016–2017 earthquakes is consistent with the trend discovered in the rupture propagation directions of the L'Aquila fault shocks and the southernmost earthquakes of the Campotosto fault (Calderoni et al., 2015). A SE-SSE rupture propagation direction was also found for the M_w 5.6 Sellano earthquake (Calderoni et al., 2011; Cultrera et al., 2008; Pino et al., 1999) and for the M_w 5.7 Colfiorito earthquake (Pino et al., 1999), both of which occurred during the 1997 Umbria-Marche seismic sequence. Therefore, an extended sector of the Apennines is characterized by a predominant trend of ruptures to the SE-SSE. Note that the M_w 6.0 Colfiorito earthquake, which is the northernmost one in Figure 5b, seems to exhibit an opposite rupture propagation direction toward the NW-NNW similar to earthquakes to the north of Campotosto up to Amatrice.

Although an explanation regarding a preferential rupture propagation direction is still controversial, the coherent behavior observed in the different sectors of the Apennines suggests a structural

origin. This may include a bimaterial fault interface (see Andrews & Ben-Zion, 1997; Brietzke, Cochard, & Igel, 2009; Bulut, Ben-Zion, & Bonhoff, 2012) or other fault properties such as low-velocity fault zone layers, as hypothesized by Ben-Zion and Huang (2002) and Brietzke and Ben-Zion (2006), or small-scale granular zones with different permeabilities (see Dunham & Rice, 2008; Rudnicki & Rice, 2006). The roles of these different factors are beyond the purpose of this paper and are currently difficult to constrain, as they can be understood only after further multidisciplinary studies ranging from laboratory experiments to geophysical prospecting and high-resolution tomography at different scales in the investigated region.

8. Concluding Remarks

We applied an EGF deconvolution technique to determine the directivity characteristics of the strongest earthquakes in the 2016–2017 central Italy seismic sequence. This approach follows the basic analysis steps of Calderoni et al. (2015) for unilateral along-strike ruptures, although it includes an original extension for additionally identifying bilateral ruptures and adopts the directivity index *D* introduced by Ross and Ben-Zion (2016) to measure the statistical significance of the different rupture typologies. The procedure is conceptually simple and fast (near real-time speeds). At the very beginning of a seismic sequence with significant earthquakes, information on the rupture directivity, at least with regard to the along-strike component, can be inferred using this approach in less than 1 h. These results can provide important constraints on hazard scenarios and future evolutionary trends of active seismic sequences in terms of their seismicity migration probabilities and strongest aftershock occurrences at short intervals.

We found that unilateral ruptures were predominant in the 2016–2017 central Italy seismic sequence (10 out of a total of 16 events). We also identified four bilateral ruptures and only two circular ruptures. The three strongest earthquakes show evidence for bilateral rupturing.

In conclusion, the direction of rupture propagation does not seem to be random. Although the number of earthquakes analyzed in this study is limited, spatially stable results are observed in different sectors of the Apennines. To the north of Amatrice up to Colfiorito, there is a predominant SE-SEE rupture trend, whereas the sector of the Apennines from the northernmost part of the Campotosto fault up to Amatrice is characterized by ruptures trending NNW-NW. Earthquakes along the southernmost part of the Campotosto fault and throughout the entire L'Aquila fault show an opposite trend with predominant ruptures trending SE similar to the Amatrice-Colfiorito sector.

Acknowledgments

Some of the figures were created using GMT (Wessel & Smith, 1991). Seismic Analysis Code (SAC) (Goldstein et al., 2003) was used for much of the analysis. Data from the DPC can be downloaded from the ITalian ACcelerometric Archive (ITACA) (http://itaca.mi.ingv.it), while data from the INGV are accessible from the European Integrated Data Archive (EIDA) (http http://eida.rm.ingv.it/) and from the Italian Seismological Instrumental and Parametric Data-Base (ISIDe) (http://iside.rm.ingv.it/). We benefited from many conversations with Elisa Tinti, Laura Scognamiglio, and Massimo Cocco, and the comparison of our results with those from different methods yielded very useful observations. We also thank Pierfrancesco Burrato for his suggestions. We thank the Editor, Yehuda Ben-Zion, in addition to Germán Prieto, Rachel Abercrombie, and Paolo Poli for their thorough reviews and very constructive critical comments.

References

Aki, K. (1967). Scaling law of seismic spectrum. *Journal of Geophysical Research*, *30*, 1217–1231.

Andrews, D. J., & Ben-Zion, Y. (1997). Wrinkle-like slip pulse on a fault between different materials. *Journal of Geophysical Research*, *102*(B1), 553–571. https://doi.org/10.1029/96JB02856

Azzaro, R., Tertulliani, A., Bernardini, F., Camassi, R., Del Mese, S., Ercolani, E., … Sbarra, M. (2016). The 24 August Amatrice 2016 earthquake: Macroseismic survey in the damage area and EMS intensity assessment. *Annales de Geophysique*, *59*, 8. https://doi.org/10.4401/ag-7203

Ben-Menahem, A. (1961). Radiation of seismic surface-waves from finite moving sources. *Bulletin of the Seismological Society of America*, *51*, 401–435.

Ben-Zion, Y., & Huang, Y. (2002). Dynamic rupture on an interface between a compliant fault zone layer and a stiffer surrounding solid. *Journal of Geophysical Research*, *107*(2042), ESE 6-1–ESE 6-13. https://doi.org/10.1029/2001JB000254

Bigi, S., Casero, P., & Ciotoli, G. (2011). Seismic interpretation of the Laga basin; constraints on the structural setting and kinematics of the central Apennines. *Journal of the Geological Society of London*, *168*(1), 179–190. https://doi.org/10.1144/0016-76492010-084

Boatwright, J. (2007). The persistence of directivity in small earthquakes. *Bulletin of the Seismological Society of America*, *97*(6), 1850–1861. https://doi.org/10.1785/0120050228

Brietzke, G. B., & Ben-Zion, Y. (2006). Examining tendencies of in-plane rupture to migrate to material interfaces. *Geophysical Journal International*, *167*(2), 807–819. https://doi.org/10.1111/j.1365-246X.2006-03137.x

Brietzke, G. B., Cochard, A., & Igel, H. (2009). Importance of bimaterial interfaces for earthquake dynamics and strong ground motion. *Geophysical Journal International*, *178*(2), 921–938. https://doi.org/10.1111/j.1365-246X.2009.04209.x

Bulut, F., Ben-Zion, Y., & Bonhoff, M. (2012). Evidence for a bimaterial interface along the Mudurnu segment of the North Anatolian fault zone from polarization analysis of *P* waves. *Earth and Planetary Science Letters*, *327-328*, 17–22. https://doi.org/10.1016/j.epsl.2012.02.001

Calderoni, G, Herrero, A., Rovelli, A., & Di Alessandro, C. (2011). Combined effect of basin resonance and source directivity: Implications for long period hazard in the Apennines, central Italy. In *Proceedings of the 4thIASPEI/IAEE International Symposium on Effects of Surface Geology on Seismic Motion*, 2011 August 23–26. Santa Barbara, CA: University of California.

Calderoni, G., Di Giovambattista, R., Vannoli, P., Pucillo, S., & Rovelli, A. (2012). Fault-trapped waves depict continuity of the fault system responsible for the 6 April 2009 M_w 6.3 L'Aquila earthquake, central Italy. *Earth and Planetary Science Letters*, *323*, 1–8.

Calderoni, G., Rovelli, A., & Singh, S. K. (2013). Stress drop and source scaling of the 2009 April L'Aquila earthquakes. *Geophysical Journal International*, *192*(1), 260–274. https://doi.org/10.1093/gji/ggs011

Calderoni, G., Rovelli, A., Ben-Zion, Y., & Di Giovambattista, R. (2015). Along-strike rupture directivity of earthquakes of the 2009 L'Aquila, central Italy, seismic sequence. *Geophysical Journal International*, *203*(1), 399–415. https://doi.org/10.1093/gji/ggv275

Carafa, M. M. C., & Bird, P. (2016). Improving deformation models by discounting transient signals in geodetic data: 2. Geodetic data, stress directions, and long-term strain rates in Italy. *Journal of Geophysical Research: Solid Earth*, *121*, 5557–5575. https://doi.org/10.1002/2016JB013038

Cheloni, D., De Novellis, V., Albano, M., Antonioli, A., Anzidei, M., Atzori, S., … Doglioni, C. (2017). Geodetic model of the 2016 central Italy earthquake sequence inferred from InSAR and GPS data. *Geophysical Research Letters*, *44*, 6778–6787. https://doi.org/10.1002/2017GL073580

Cultrera, G., Pacor, F., Franceschina, G., Emolo, A., & Cocco, M. (2008). Directivity effects for moderate-magnitude earthquakes (M_w 5.6–6.0) during the 1997 Umbria–Marche sequence, central Italy. *Tectonophysics*, *476*(1-2), 110–120. https://doi.org/10.1016/j.tecto.2008.09.022

Devoti, R., Esposito, A., Pietrantonio, G., Pisani, A. R., & Riguzzi, F. (2011). Evidence of large scale deformation patterns from GPS data in the Italian subduction boundary. *Earth and Planetary Science Letters*, *311*(3-4), 230–241. https://doi.org/10.1016/j.epsl.2011.09.034

DISS Working Group (2015). Database of Individual Seismogenic Sources (DISS), version 3.2.0: A compilation of potential sources for earthquakes larger than *M* 5.5 in Italy and surrounding areas. Retrieved from http://diss.rm.ingv.it/diss/, Istituto Nazionale di Geofisica e Vulcanologia; https://doi.org/10.6092/INGV.IT-DISS3.2.0

Dunham, E. M., & Rice, J. R. (2008). Earthquake slip between dissimilar poroelastic materials. *Journal of Geophysical Research*, *113*, B09304. https://doi.org/10.1029/2007JB005405

Folesky, J., Kummerow, J., Shapiro, S. A., Häring, M., & Asanuma, H. (2016). Rupture directivity of fluid induced microseismic events: Observations from an enhanced geothermal system. *Journal of Geophysical Research: Solid Earth*, *121*, 8034–8047. https://doi.org/10.1002/2016JB013078

Galadini, F., & Galli, P. (2003). Paleoseismology of silent faults in the central Apennines (Italy): The Mt. Vettore and Laga Mts. Faults. *Annales de Geophysique*, *46*, 815–836.

Ghisetti, F., & Vezzani, L. (1991). Thrust belt development in the central Apennines (Italy): Northward polarity of thrusting and out-of-sequence deformations in the Gran Sasso Chain. *Tectonics*, *10*(5), 904–919. https://doi.org/10.1029/91TC00902

Goldstein, P., Dodge, D., Firpo, M., & Minner, L. (2003). SAC2000: Signal processing and analysis tools for seismologists and engineers. In W. H. K. Lee, et al. (Eds.), *Invited contribution to "The IASPEI International Handbook of Earthquake and Engineering Seismology"*. Academic Press. https://doi.org/10.1016/S0074-6142(03)80284-X

Haskell, N. A. (1964). Total energy spectral density of elastic wave radiation from propagating faults. *Bulletin of the Seismological Society of America*, *54*, 1811–1841.

Hirasawa, T., & Stauder, W. (1965). On the seismic body waves from a finite moving source. *Bulletin of the Seismological Society of America*, *55*, 237–262.

Kane, D. L., Shearer, P. M., Goertz-Allmann, B. P., & Vernon, F. L. (2013). Rupture directivity of small earthquakes at Parkfield. *Journal of Geophysical Research: Solid Earth*, *118*, 212–221. https://doi.org/10.1029/2012JB009675

Koketsu, K., Miyake, H., Guo, Y., Kobayashi, H., Masuda, T., Davuluri, S., … Sapkota, S. N. (2016). Widespread ground motion distribution caused by rupture directivity during the 2015 Gorkha, Nepal earthquake. *Scientific Reports*, *6*(1), 28536. https://doi.org/10.1038/srep28536

Lavecchia, G., Castaldo, R., de Nardis, R., De Novellis, V., Ferrarini, F., Pepe, S., … Tizzani, P. (2016). Ground deformation and source geometry of the August 24, 2016 Amatrice earthquake (central Italy) investigated through analytical and numerical modeling of DInSAR measurements and structural-geological data. *Geophysical Research Letters*, *43*, 12,389–12,398. https://doi.org/10.1002/2016GL071723

Lengliné, O., & Got, J.-L. (2011). Rupture directivity of micro-earthquake sequences near Parkfield, California. *Geophysical Research Letters*, *38*, L08310. https://doi.org/10.1029/2011GL047303

López-Comino, J. A., Stich, D., Morales, J., & Ferreira, A. M. G. (2016). Resolution of rupture directivity in weak events: 1-D versus 2-D source parameterizations for the 2011, M_w 4.6 and 5.2 Lorca earthquakes, Spain. *Journal of Geophysical Research: Solid Earth*, *121*, 6608–6626. https://doi.org/10.1002/2016JB013227

McGuire, J. (2004). Estimating the finite source properties of small earthquake ruptures. *Bulletin of the Seismological Society of America*, *94*(2), 377–393. https://doi.org/10.1785/0120030091

Michele, M., Di Stefano, R., Chiaraluce, L., Cattaneo, M., De Gori, P., Monachesi, G., … Fares, M. (2016). The Amatrice 2016 seismic sequence: A preliminary look to the main shock and aftershocks distribution. *Annales de Geophysique*, *59*, 8. https://doi.org/10.4401/ag-7227

Park, S., & Ishii, M. (2015). Inversion for rupture properties based upon 3-D directivity effect and application to deep earthquakes in the Sea of Okhotsk region. *Geophysical Journal International*, *203*(2), 1011–1025. https://doi.org/10.1093/gji/ggv352

Pierantoni, P., Deiana, G., & Galdenzi, S. (2013). Stratigraphic and structural features of the Sibillini Mountains (Umbria-Marche Apennines, Italy). *Italian Journal of Geosciences*, *132*(3), 497–520. https://doi.org/10.3301/IJG.2013.08

Pino, N. A., Mazza, S., & Boschi, E. (1999). Rupture directivity of the major shocks in the 1997 Umbria–Marche (central Italy) sequence from regional broadband waveforms. *Geophysical Research Letters*, *26*, 2101–2104. https://doi.org/10.1029/1999GL900464

Poli, P., Prieto, G. A., Yu, C. Q., Florez, M., Agurto-Detzel, H., Mikesell, T. D., … Pedraza, P. (2016). Complex rupture of the *M*6.3 2015 March 10 Bucaramanga earthquake: Evidence of strong weakening process. *Geophysical Journal International*, *205*(2), 988–994. https://doi.org/10.1093/gji/ggw065

Prieto, G. A., Froment, B., Yu, C., Poli, P., & Abercrombie, R. (2017). Earthquake rupture below the brittle-ductile transition in continental lithospheric mantle. *Science Advances*, *3*, e1602642. https://doi.org/10.1126/sciadv.1602642

Pucci, S., De Martini, P. M., Civico, R., Villani, F., Nappi, R., Ricci, T., … Pantosti, D. (2017). Coseismic ruptures of the 24 August 2016, M_w 6.0 Amatrice earthquake (central Italy). *Geophysical Research Letters*, *44*, 2138–2147. https://doi.org/10.1002/2016GL071859

Ross, Z. E., & Ben-Zion, Y. (2016). Toward reliable automated estimates of earthquake source properties from body wave spectra. *Journal of Geophysical Research: Solid Earth*, *121*, 4390–4407. https://doi.org/10.1002/2016JB013003

Rubin, A., & Gillard, D. (2000). Aftershock asymmetry/rupture directivity along central San Andreas Fault microearthquakes. *Journal of Geophysical Research*, *105*(B8), 19,095–19,109. https://doi.org/10.1029/2000JB900129

Rudnicki, J. W., & Rice, J. R. (2006). Effective normal stress alteration due to pore pressure changes induced by dynamic slip propagation on a plane between dissimilar materials. *Journal of Geophysical Research*, *111*, B10308. https://doi.org/10.1029/2006JB004396

Scisciani, V., Agostini, S., Calamita, F., Pace, P., Cilli, A., Giori, I., & Paltrinieri, W. (2014). Positive inversion tectonics in foreland fold-and-thrust belts: A reappraisal of the Umbria–Marche northern Apennines (central Italy) by integrating geological and geophysical data. *Tectonophysics*, *637*, 218–237. https://doi.org/10.1016/j.tecto.2014.10.010

Seekins, L. C., & Boatwright, J. (2010). Rupture directivity of moderate earthquakes in Northern California. *Bulletin of the Seismological Society of America*, *100*(3), 1107–1119. https://doi.org/10.1785/0120090161

Tinti, E., Scognamiglio, L., Michelini, A., & Cocco, M. (2016). Slip heterogeneity and directivity of the M_L 6.0, 2016, Amatrice earthquake estimated with rapid finite-fault inversion. *Geophysical Research Letters*, *43*, 10,745–10,752. https://doi.org/10.1002/2016GL071263

Tinti, E., Scognamiglio, L., Magnoni, F., Casarotti, E., Michelini, A., & Cocco, M. (2017). Rupture complexity of the three main shocks of the 2016 central Italy seismic sequence. *Geophysical Research Abstracts,19*, EGU2017–16925.

Warren, L. M., & Shearer, P. M. (2006). Systematic determination of earthquake rupture directivity and fault planes from analysis of long-period *P*-wave spectra. *Geophysical Journal International*, *164*(1), 46–62. https://doi.org/10.1111/j.1365-246X.2005.02769.x

Wessel, P., & Smith, W. H. F. (1991). Free software helps map and display data. *Eos, Transactions of the American Geophysical Union*, *72*(41), 441. https://doi.org/10.1029/90EO00319

Zaliapin, I., & Ben-Zion, Y. (2011). Asymmetric distribution of aftershocks on large faults in California. *Geophysical Journal International*, *185*(3), 1288–1304. https://doi.org/10.1111/j.1365-246X.2011.04995.x